


Sidewall Quantum Wires on GaAs(001) Substrates

Paul L.J. Helgers,^{1,2,*} Haruki Sanada,² Yoji Kunihashi,² Antonio Rubino,³ Christopher J.B. Ford,³ Klaus Biermann,¹ and Paulo V. Santos¹

¹*Paul-Drude-Institut für Festkörperelektronik, Leibniz-Institut im Forschungsverbund Berlin e. V., Hausvogteiplatz 5-7, 10117 Berlin, Germany*

²*NTT Basic Research Laboratories, NTT Corporation, 3-1 Morinosato-Wakamiya, Atsugi, Kanagawa 243-0198, Japan*

³*Cavendish Laboratory, University of Cambridge, J. J. Thomson Avenue, Cambridge CB3 0HE, UK*

 (Received 10 January 2019; revised manuscript received 8 May 2019; published 10 June 2019)

We study the structural, optical, and transport properties of sidewall quantum wires (QWRs) on GaAs(001) substrates. QWRs are grown by MBE on GaAs(001) substrates prepatterned with shallow ridges. They form as a consequence of material accumulation on the sidewalls of the ridges during the overgrowth of a quantum well (QW) on the patterned surface. The QWRs are approximately 200 nm wide and have emission energies red shifted by 27 meV with respect to the surrounding QW. Spatially resolved spectroscopic PL studies indicate that the QW thickness reduces around the QWRs, thus creating a 4-meV energy barrier for the transfer of carriers from the QW to the QWR. We show that the QWRs act as efficient channels for the transport of optically excited electrons and holes over tens of μm by a high-frequency surface acoustic wave (SAW). These results demonstrate the feasibility of efficient ambipolar transport in QWRs with submicrometer dimensions, photolithographically defined on GaAs substrates.

DOI: [10.1103/PhysRevApplied.11.064017](https://doi.org/10.1103/PhysRevApplied.11.064017)

I. INTRODUCTION

Planar quantum wires (QWRs) are important components for the realization of interconnects for integrated optical-electronic circuits. In its simplest form, the guiding action by the lateral confinement of carriers enables information exchange between two remote locations via a well-defined channel. The mesoscopic confinement induced by small lateral dimensions can be explored for additional functionalities. Here, interesting examples are the formation of one-dimensional quantum channels for electronic transport with reduced scattering [1], as well as the enhanced spin lifetimes due to mesoscopic spin confinement [2,3].

Different approaches have been reported for the fabrication of semiconductor QWRs with nanometer dimensions. Electrostatically defined QWRs can be created via the deposition of gates on a semiconductor nanostructure. The application of a voltage to the gate creates channels near the surface for one type of carrier (i.e., electrons or holes). Ambipolar transport channels for the guidance of both electrons and holes by moving acoustic fields can be created by combining electrostatic gates with piezoelectricity [4]. More interesting for electro-optical applications are planar QWRs defined by a lateral structural modulation since these have optical resonance energies distinct from

the ones of the surrounding matrix. In its simplest form, the structural modulation can be introduced by etching a QW sample to define the QWR. Alternatively, a QWR can be formed by the epitaxial growth of a QW structure on a surface with a predefined structural modulation. Here, one example is given by QWRs produced by the epitaxial growth on the cleaved edge of a nanostructure containing a QW [5]. A second example is provided by the epitaxial growth on a surface exposing different crystallographic orientations: here, one takes advantage of the dependence of the growth kinetics on the orientation of the surface in order to create the lateral structural modulation. Surface structuring in this case is usually achieved by pre-etching the substrate surface to expose different crystallographic facets. Well-known examples are QWRs grown by metal-organic epitaxy on V-shaped grooves defined on a GaAs(001) surface [6–8], as well as quantum wires and dots fabricated by MBE on (111) [9], (001) [10], and (113) GaAs surfaces [11–13].

An advantage of the growth-defined QWRs over those defined by etching resides on the fact that they do not contain free surfaces, which may be deleterious for electronic excitations. In addition, and in contrast to their electrostatic counterparts, these QWRs are fully surrounded by epitaxial materials and can therefore be easily embedded in more complex epitaxial structures such as optical microcavities. The formation of QWRs via MBE growth has so far only been demonstrated for few crystallographic orientations of

*helgers@pdi-berlin.de

the growth surface. The formation of sidewall QWRs via MBE overgrowth on patterned GaAs(001) substrates was reported by Lee *et al.* [10]. Studies of these sidewall QWRs have, however, only addressed structural properties. The objective of this paper is to extend the structural analysis with respect to Ref. [10], as well as to provide a systematic investigation of the optical and transport properties of these QWRs, which have, to our knowledge, so far not been addressed. From the point of view of applications, the GaAs(001) surface is the most technologically relevant orientation for MBE growth. MBE growth on this surface is better understood and controlled than on high-index surfaces such as GaAs(113)A.

One important application of planar QWRs is as guides and interconnects for photoexcited electron-hole pairs between opto-electronic structures on a surface. In this paper, we investigate the transport properties of the QWRs by using SAWs to move optically excited carriers along the QWR axis. The moving piezoelectric field of a SAW creates a periodic type-II modulation of the material's band edges, which stores electrons and holes in spatially separated locations and transports them along the sample surface [14,15]. After transport, the carriers can be forced to recombine and emit photons, thus providing a photonic interface to the electronic system. The ambipolar acoustic transport by SAWs thus provides a convenient approach for probing the transport properties in nanostructures without the need of doping or electrical contacts. Similar ambipolar acoustic transport studies were carried out in μm -sized electrostatically defined wires [16] as well as sub- μm sidewall QWRs fabricated by epitaxially overgrowing shallow ridges on GaAs(113)A substrates [17,18]. Long acoustically driven transport distances for charge carriers have been achieved in overgrown QWRs (up to $50\ \mu\text{m}$) [19]. Their optical and transport properties were found, however, to be very sensitive to potential fluctuations along the transport path. These fluctuations create trapping centers, which can capture charge carriers during the acoustically driven ambipolar transport and induce their recombination, thus resulting in a reduction of the acoustic transport efficiency [20].

The one-directional motion of carriers in QWRs also provides a pathway to reduce spin dephasing due to the Dyakonov-Perel mechanism [2,3]. Alsina *et al.* [19] investigated spin transport in sidewall QWRs grown on GaAs(113)A substrates with a width of $50\ \text{nm}$. Whereas the narrow width should lead to a long spin-relaxation time and, correspondingly, long spin-transport lengths, the observed acoustic spin-transport length is limited to distances of only approximately $2\ \mu\text{m}$. These transport distances are much shorter than the ones reported for acoustic transport in electrostatic wires [21]. It was argued that the acoustic spin-transport length is limited by Elliot-Yafet (EY) scattering due to the large density of scattering

centers along the QWR axis [19]. These findings call for fabrication processes yielding narrow QWRs with small potential fluctuations.

In this contribution, we provide a systematic investigation of the structural, optical, and acoustic transport properties of sidewall QWRs fabricated on GaAs(001) substrates. The QWR fabrication process used in the present studies, which includes substrate patterning and MBE growth, is based on the previous work in Ref. [10] and is summarized in Sec. II A. Sections II B and II C then describe the procedures for the fabrication of interdigital transducers for SAW generation and the spectroscopic techniques employed in the studies. The experimental results are presented in Sec. III. Here, we start by studying the structural properties of the QWRs by combining atomic force microscopy (AFM), SEM, and STEM (Sec. III A). We then carry out spectroscopic investigations of the QWR optical properties using spatially resolved PL (Secs. III B–III D). Finally, Sec. III E provides evidence for the acoustic charge transport in the QWRs over distances approaching $100\ \mu\text{m}$. Section IV summarizes the main conclusions drawn in this work.

II. EXPERIMENTAL DETAILS

A. Sample fabrication

The fabrication of the sidewall QWRs on GaAs(001) substrates followed a procedure similar to the ones reported in Refs. [11] [GaAs(113)A] and [10] [GaAs(001)]. In the first step, shallow ridges are patterned on a GaAs(001) substrate by photolithography and wet chemical etching using a solution of $\text{H}_2\text{SO}_4:\text{H}_2\text{O}_2:\text{H}_2\text{O}$ with a volume ratio of (8:1:100). We fabricate $10\text{-}\mu\text{m}$ -wide ridges with a height of $45\ \text{nm}$ and a length of several tens of μm oriented along the $y||[110]$ and $x||[\bar{1}\bar{1}0]$ main axes of the GaAs(001) surface. The patterned substrate is subsequently cleaned using a $\text{H}_2\text{SO}_4:\text{H}_2\text{O}$ (96:4) solution and introduced in a UHV chamber connected to the MBE growth apparatus for surface cleaning by exposure to atomic hydrogen. In this procedure, the substrate is exposed to partially cracked hydrogen from a hot filament source at a background pressure of 5×10^{-5} mbar for 30 min at a temperature of $450\ ^\circ\text{C}$. The sample is then transferred in vacuum to the MBE growth chamber. Figure 1(a) schematically shows the formation of QWRs (red areas) after the overgrowth of a layer structure, consisting of a 10-nm QW (blue) sandwiched between a lower and upper $\text{Al}_{0.15}\text{Ga}_{0.85}\text{As}$ barrier with thicknesses of, respectively, 130 and $200\ \text{nm}$. The $\text{Al}_{0.15}\text{Ga}_{0.85}\text{As}$ barriers have been omitted for clarity. For comparison, a sample containing QWRs on a GaAs(113)A substrate has been fabricated following a similar procedure, using an $\text{H}_2\text{SO}_4:\text{H}_2\text{O}_2:\text{H}_2\text{O}$ etching solution with a volume ratio of (1:8:100). For both types of samples, all layers are grown while the substrate is kept at a temperature of $600\ ^\circ\text{C}$. The growth rate of

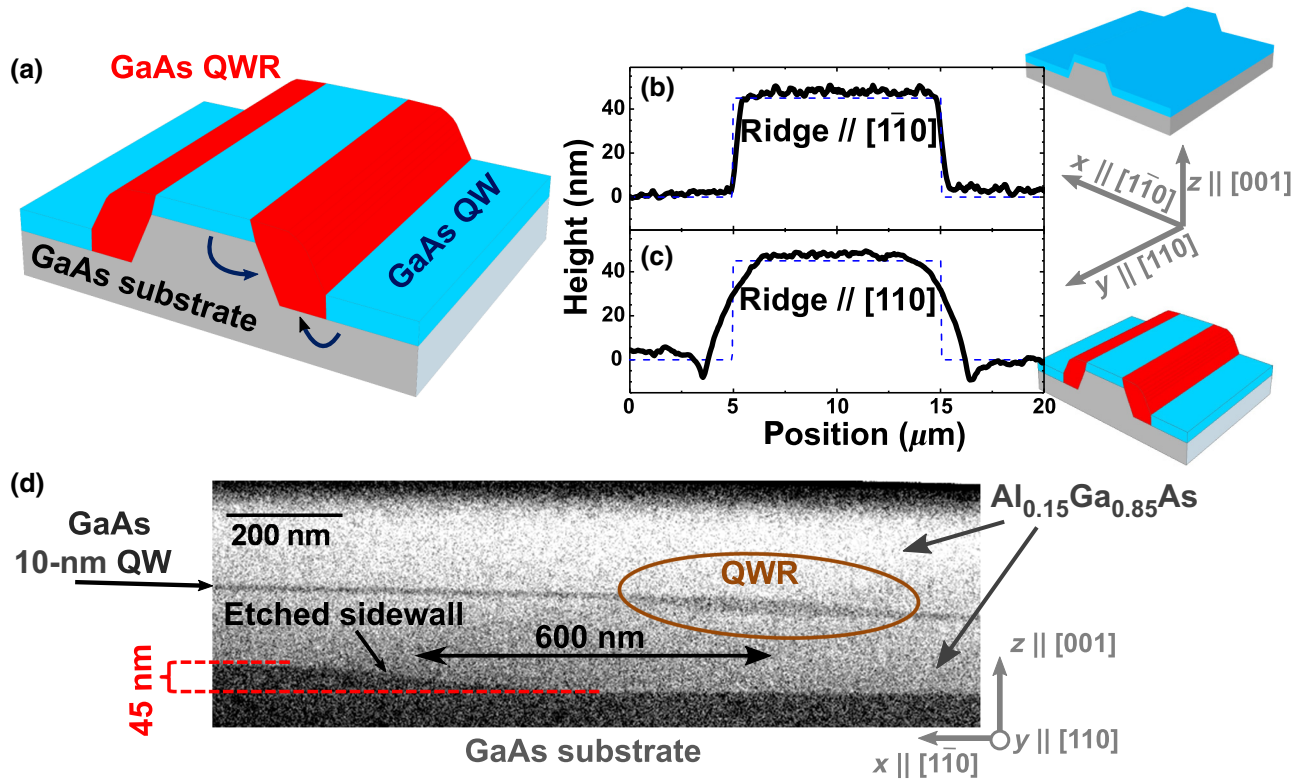


FIG. 1. MBE of sidewall QWRs on GaAs(001). (a) Shallow ridges (height of approximately 45 nm) are patterned on a GaAs(001) substrate and subsequently overgrown with a QW (blue areas). Arrows show the preferential diffusion of Ga adatoms towards the ridge sidewall, which results in the formation of a QWR (red regions). For clarity, the $\text{Al}_{0.15}\text{Ga}_{0.85}\text{As}$ QW barriers have been omitted. (b),(c) AFM cross-sectional profiles of overgrown ridges oriented along the (b) $x \parallel [1\bar{1}0]$ and (c) $y \parallel [110]$ directions of the GaAs(001) surface. The blue dashed lines indicate the contour of prepatterned ridges defined by optical lithography. The pronounced lateral growth results in QWR formation only along the y -oriented sidewalls. (d) Cross-sectional STEM image of an overgrown ridge showing the QW (GaAs, dark layer) sandwiched between two $\text{Al}_{0.15}\text{Ga}_{0.85}\text{As}$ barriers (bright layers). The brown circle highlights the region of increased QW thickness defining the sidewall QWR.

the $\text{Al}_{0.15}\text{Ga}_{0.85}\text{As}$ and GaAs layers is, respectively, 0.16 and 0.14 nm s^{-1} . Finally, the samples are capped with a 2-nm layer of GaAs in order to protect the sample against oxidation.

The formation of QWRs on the ridge sidewalls relies on the combination of two factors [10,22–24]: (i) the higher adatom diffusion rate along the $x \parallel [1\bar{1}0]$ surface direction of the (2×4) reconstructed GaAs(001) surface as compared to the $y \parallel [110]$ direction and (ii) the higher adatom incorporation rate at step edges oriented along y as compared to the plane (001) surface. The latter results in an enhanced MBE growth rate on the exposed sidewalls of the ridges as compared to the growth rate on the (001) surface. When a QW is deposited on the patterned surface, the anisotropic growth rate induces a local increase in the QW thickness on the sidewalls of ridges aligned along the y direction [10], as indicated by the red regions in Fig. 1(a). The structural properties of the overgrown ridges are investigated by combining AFM, SEM, and STEM.

B. Excitation of SAWs

Figure 2(a) displays the layout of the delay line used for the excitation of Rayleigh SAWs [25] along the QWR axis. The delay line is fabricated by optical lithography on the surface of the overgrown sample: it consists of two split-finger interdigital transducers (IDTs) designed for an acoustic wavelength $\lambda_{\text{SAW}} = 5.6 \mu\text{m}$ with aperture and length of $120 \mu\text{m}$ and $350 \times \lambda_{\text{SAW}}$, respectively. Figures 2(b) and 2(c) show the frequency dependence of the radio-frequency (rf) reflection (s_{11}) and transmission (s_{21}) parameters at room temperature, respectively. The resonance at 513 MHz corresponds to the excitation of the Rayleigh mode for the structure. The amplitude of the s_{11} dip indicates that the IDTs convert 20% of the input rf power into two SAW modes propagating in opposite directions. The $r_{\text{IDT}} = 10\%$ transduction per SAW beam is compatible with the maximum power transmission amplitude of the s_{12} spectrum of -20 dB . Experiments are also carried out using IDTs for an acoustic wavelength $\lambda_{\text{SAW}} = 4 \mu\text{m}$, resulting in a SAW frequency of $f_{\text{SAW}} = 726 \text{ MHz}$.

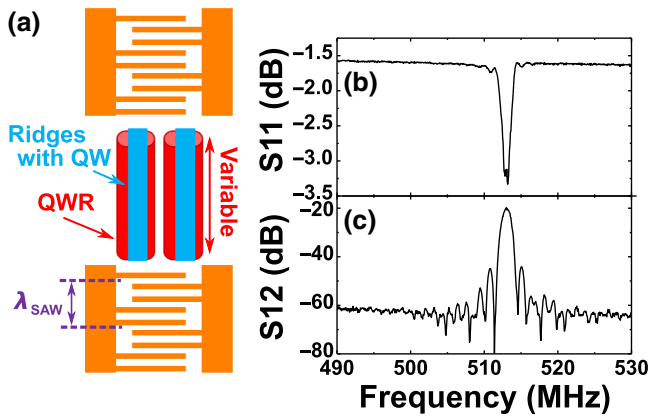


FIG. 2. (a) Schematic diagram of the SAW delay line embedding sidewall QWRs aligned along the $y \parallel [110]$ direction of the GaAs(001) substrate. The delay line consists of two IDTs with an aperture of 120 μm and acoustic wavelength $\lambda_{\text{SAW}} = 5.6 \mu\text{m}$. (b) rf reflection (s_{11}) and (c) rf transmission (s_{21}) parameters for the delay line measured at room temperature. The resonance at 513 MHz is associated with the excitation of the Rayleigh SAW mode of the sample structure.

C. Optical spectroscopy techniques

The spectroscopic PL studies are carried out using an optical microscope coupled to a cryostat (temperature of approximately 10 K) with optical access and rf wiring for the excitation of SAWs. The PL is excited by either a cw or pulsed tunable Ti:sapphire laser, or by a pulsed diode laser ($\lambda_{\text{diode}} = 635 \text{ nm}$). The PL around the excitation spot is spectrally analyzed and detected with a spatial resolution of 0.5 μm per pixel by a cooled CCD camera. Time-resolved measurements are performed using either a streak camera or an avalanche Si photodiode as a detector.

The acoustic transport studies are carried out by exciting one of the IDTs of the delay line. The electron-hole pairs are excited by a focused laser spot on one position of the sample [cf. Fig. 2(a)] and their spatial distribution along the SAW propagation direction detected by recording spatially resolved PL profiles. The amplitude of the SAW is stated in terms of the nominal rf power applied to the rf input of the cryostat. Note that the electroacoustic conversion efficiency in the cryostat will be lower than the one determined in Fig. 2, which does not take into account the effects of the cryostat rf connections.

III. RESULTS AND DISCUSSION

A. Structural properties

Since MBE is a nonconformal growth technique, the shape of the ridges can be recovered by probing the sample surface after overgrowth using AFM. The solid lines in Figs. 1(b) and 1(c) compare cross-sectional AFM profiles of overgrown ridges oriented along the x and y directions, respectively. The blue dashed lines indicate the

nominal profiles of the ridge etched on the surface prior to the MBE overgrowth. The cross-sectional profile of overgrown ridges oriented along the x direction closely follows the one prepatterned on the surface, thus indicating a conformal coverage during the MBE overgrowth. Ridges oriented along y exhibit, in contrast, broadened sidewalls with a convex shape. This behavior is attributed to the higher growth rates at the edge of these ridges, which results in material accumulation along their sidewalls. This material accumulation locally increases the thickness of a QW overgrown on the ridge edges, thus forming the region with lower quantum-confinement energy, corresponding to the QWR [cf. Fig. 1(a)].

The material transfer leading to QWR formation also reduces the thickness of the QW regions adjacent to the sidewalls. As discussed in detail in Sec. III B, this local thickness decrease creates a “barrier QW” with higher carrier confinement energies than in the QW on both sides of the QWR. These “barrier QWs” act as potential barriers for the transfer of carriers from the QW to the QWR.

The sidewall QWRs only form on overgrown ridges oriented along y . These can be directly imaged in cross-sectional STEM images, as illustrated in Fig. 1(d). Here, the dark and bright areas correspond to GaAs and $\text{Al}_{0.15}\text{Ga}_{0.85}\text{As}$ regions, respectively. From the micrographs, we estimate the thickness and width of the sidewall QWR to be 25 ± 5 and 200 ± 5 nm, respectively. The QWR is thus approximately 2.5 times thicker than the deposited 10-nm QW. Interestingly, the QWR does not form directly on the location of the ridge sidewall on the substrate, but is shifted by approximately 600 nm. From the ratio between the 600-nm lateral shift and the 130 nm thickness of the lower $\text{Al}_{0.15}\text{Ga}_{0.85}\text{As}$ barrier, we estimate that for this particular geometry the lateral growth rate of the $\text{Al}_{0.15}\text{Ga}_{0.85}\text{As}$ layer is approximately five times larger than the vertical one.

The electro-optical properties and, in particular, the carrier transport properties of the sidewall QWRs also depend on the uniformity of the QWR dimensions along both the growth direction and the QWR axis direction. The latter can be quantified by evaluating the lateral roughness of the ridge edges (line-edge-roughness, LER) from AFM micrographs. For that purpose, we record AFM profiles across patterned ridges aligned along y (typically one profile per nanometer). An AFM micrograph of a ridge sidewall wet-chemically etched on the GaAs(001) substrate (i.e., prior to MBE overgrowth) is shown in Fig. 3(a). Here, the dark area corresponds to the ridge bottom (etched) and the bright area to the ridge top (nonetched). The right panel displays a typical profile, extracted along the vertical dashed green line in the AFM image. Each of these profiles is fitted with an error function to evaluate the average position of the ridge edge. LER is defined as the standard deviation of the edge position. Figure 3(b) shows the same scan as Fig. 3(a), now enlarged into an area of 1 $\mu\text{m} \times 80 \text{ nm}$.

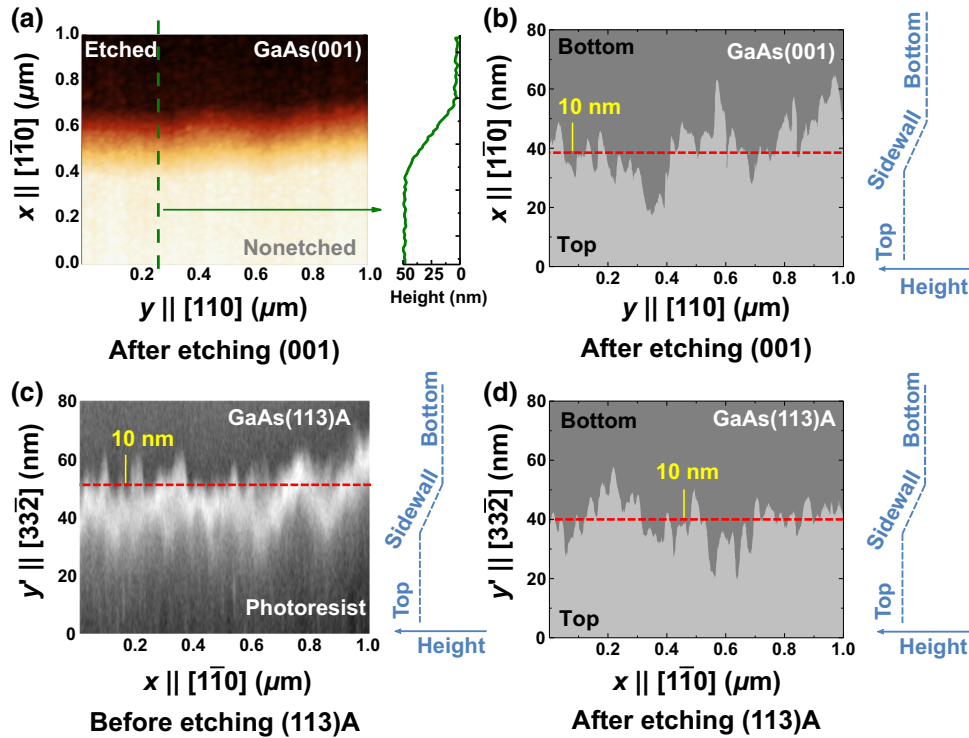


FIG. 3. LER of ridges fabricated on GaAs substrates. (a) AFM scan of a $1 \times 1 \mu\text{m}^2$ -sized area around a ridge sidewall after etching and before MBE overgrowth. The right panel shows a profile extracted along the green dashed vertical line. (b) Postprocessed image of the same scan, enlarged into a $1 \mu\text{m} \times 80 \text{ nm}$ -sized area. The ridge bottom is dark gray and its top is bright gray. The red dashed line depicts the average position of the step edge, yielding a LER of 9 nm. (c) SEM of the photoresist defining the ridges after resist exposure to UV light of 250 nm (but before etching). The upper part of the image corresponds to a GaAs(113)A substrate and the lower part of the image corresponds to the photoresist. The rms LER value of 10 nm is comparable to the deviations observed in the ridge shown in (d). (d) Postprocessed image of an AFM scan of a $1 \mu\text{m} \times 80 \text{ nm}$ -sized area around a ridge sidewall on a GaAs(113)A substrate after etching and before MBE overgrowth. The LER of ridges on GaAs(113)A (approximately 7 nm for the shown measurement) has a similar amplitude as on GaAs(001).

The image is postprocessed to show only the heights of the ridge top and bottom. The edge position, which is depicted by the red dashed line dividing the top and bottom areas, fluctuates with peak amplitudes of as much as 20 nm and shows a LER value of 9 nm. Furthermore, we observe that the sidewall of the ridge is inclined by an angle of roughly 10° with respect to the surface plane.

Interestingly, the LER of ridges on GaAs(001) substrates is found to be approximately the same as in control samples deposited on GaAs(113)A substrates [cf. Fig. 3(d)]: in both cases, we measure LER in the range from 4 to 9 nm.

The LER could not be reduced by changing the composition of the etching solution (i.e., the type of acid agent as well as the degree of dilution of the etching solvent). We find, in contrast, that the LER can be traced back to the photolithography process used to define the ridges. In fact, SEM images of the photoresist edges at GaAs(113)A [cf. Fig. 3(c)] display LER values very similar to the ones measured after overgrowth [cf. Fig. 3(d)]. Several factors leading to the LER of photoresist patterns are discussed in detail in Ref. [26].

Attempts are also carried out to improve the LER of the sidewalls using patterns defined by e-beam lithography. Ridges defined on a GaAs(113)A substrate by e-beam lithography using a step size of 20 nm and an Allresist ARP 6200 resist have LERs similar to the ones obtained by optical lithography. By reducing the stepsize of the e-beam lithography to 2 nm and using a PMMA resist (950 K A4 1:1 Anisole), the LER could be reduced to approximately 3 nm, thus indicating a way to improve the ridge quality.

Note that since the LER is only a few percent of the width of the sidewall QWR determined by STEM [see Fig. 1(d)], we expect that it will only play a minor role in the optical, electrical, and transport properties of the sidewall QWRs. Unless otherwise specified, the results presented here are obtained on QWRs fabricated on photolithographically defined ridges.

B. Optical properties of the QWRs

The formation of QWRs at the ridge sidewall is verified by spatially resolved PL spectroscopy. Figure 4(a) displays a PL map recorded at 10 K while scanning a laser spot

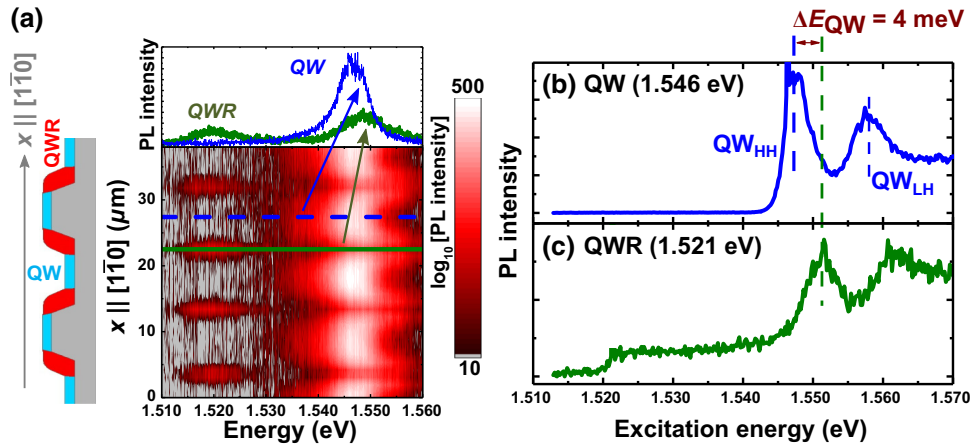


FIG. 4. (a) PL map recorded while scanning the excitation laser spot in the direction perpendicular to two $10\text{-}\mu\text{m}$ -wide ridges with sidewall QWRs (cf. left panel). The map shows the color-coded PL intensity (in a logarithmic scale) as a function of position (vertical axis) and emission energy (horizontal axis). Emission is observed from two distinct resonances. The low energy corresponds to the QWR emission and the high energy corresponds to the QW. The upper panel shows spectra along the cross sections of the PL map indicated by the horizontal lines, where the QW spectrum depicts the spectrum extracted along the dashed blue line. Figures (b) and (c) show PL excitation (PLE) spectra detected at the electron-heavy-hole resonance for the (b) QW (QW_{HH}) and (c) QWR (QWR_{HH}). In both cases, the excitation spot is placed on a sidewall QWR.

across ridges with sidewall QWRs (cf. left panel). We use for excitation a pulsed diode laser emitting at a wavelength of 635 nm . The latter lies above the fundamental optical transitions of the QW and, thus, optically excites carriers both in the QW and the QWR. The scan length covers two $10\text{-}\mu\text{m}$ -wide overgrown ridges separated from each other by $10\text{ }\mu\text{m}$. The map is generated by spectrally analyzing, for each spot position, the PL emitted within a $1.5 \times 2\text{ }\mu\text{m}^2$ area around it. The procedure yields the PL map with the color-coded intensity in a logarithmic scale as a function of position (vertical axis) and energy (horizontal axis). The upper panel displays spectral cross sections of the map recorded along the blue dashed (QW at ridge top) and green solid (sidewall QWR) horizontal lines indicated in the map.

The PL map of Fig. 4(a) shows two main resonances. Spectra recorded on the top and bottom of the ridges are essentially equal and characterized by a single PL line centered at 1.547 eV with a linewidth (defined as the FWHM) of 7 meV . This line is attributed to the electron-heavy hole (QW_{HH}) resonance of the 10 nm QW. Spectra recorded on the sidewall display, in addition, a second resonance at 1.520 eV with a linewidth of 10.5 meV , which is assigned to the electron-heavy-hole transition of the QWR (QWR_{HH}). As discussed in Sec. III A, the width of the QWR is much larger (approximately 200 nm) than its thickness (approximately 25 nm). The red shift of the QWR emission with respect to the QW is, therefore, mainly caused by its larger thickness with respect to the QW. Furthermore, due to its increased thickness, one expects a decrease of the QWR linewidth with respect to the QW. The opposite trend observed in the experiments

implies that potential fluctuations within the QWR have a significant impact, possibly related to the aforementioned LER. The fact that the QWR_{HH} resonance is only seen at the sidewall positions (see left panel) also confirms the structural findings of Sec. III A that the QWRs only form at the sidewalls.

A closer analysis of the PL spectra recorded at the sidewalls reveals that the QW line reduces in intensity and slightly blue shifts (by approximately 3 meV) with respect to spectra taken at a position away from the ridges (not shown here). The blue-shifted region is attributed to the “barrier QWs” with reduced thickness formed on both sides of the sidewall QWR. Electron-hole pairs photoexcited within the barrier QW can diffuse to and recombine in the neighboring regions of lower energy. The blue-shifted PL emission at the ridge sidewall in Fig. 4(a) is symmetric with respect to the axis of the QWR, thus proving that the barrier QW forms an energy barrier for the transfer of carriers from the QW to the QWR on both sides of the QWR. Considering that the dimension of the sidewalls is much smaller than the optical resolution, the PL line in Fig. 4(a) includes contributions from both the barrier QW and the QW. The latter may be responsible for the increased linewidth of the QW PL to 11 meV on the sidewall as compared to 7 meV measured away from the sidewall.

C. Comparison with other sidewall QWRs

Table I compares the optical properties of sidewall QWRs grown on GaAs(001) substrates with QWRs grown on GaAs(113)A substrates. The table is constructed using

TABLE I. Comparison of the optical properties of sidewall QWRs on (001) and (113) GaAs substrates. The last column lists the corresponding properties for V-groove QWRs on (111) (from Ref. [8]). ΔE_{QWR} denotes the red shift of the QWR PL line with respect to the QW line.

	(001)	(113)A	(113)A e beam	(111) V groove
QW width (nm)	10	10	8	7
E_{QWR} (eV)	1.520	1.526	1.546	1.575
ΔE_{QWR} (meV)	27	15	13	45
linewidth ^a (meV)	10	11	9	11

^aDefined as the FWHM.

average values of the emission energies and linewidths of QWRs from multiple samples simultaneously grown on the same 2-inch wafer, per substrate type. The fourth column displays the emission energies and linewidths of QWRs fabricated on e-beam lithographic defined ridges on a GaAs(113)A substrate overgrown with a slightly thinner QW (8 nm instead of 10 nm). Interestingly, all sidewall QWRs have similar spectral linewidths of 10 ± 1 meV. The energetic separation ΔE_{QWR} between the QW and the QWR emission energies, in contrast, is significantly larger for QWRs on GaAs(001) than on GaAs(113)A and leads to a larger carrier confinement for GaAs(001). This larger red shift, which is probably related to the different sidewall facets exposed by the etching process, is advantageous for carrier transport since it reduces the carrier-escape probability to the surrounding QW. Finally, the last column of the table lists the corresponding properties for V-groove QWRs deposited by Koshiba *et al.* on GaAs(111) substrates (from Ref. [8]). These QWRs have a linewidth comparable to the ones for the sidewall QWRs but substantially larger energetic separations ΔE_{QWR} .

D. Carrier dynamics in GaAs(001) QWRs

In order to investigate carrier transfer between the QW and the QWR, we measure PLE from the sidewalls using a tunable cw Ti:sapphire laser impinging on the sidewall region at an angle of incidence of 45° . The laser spot size of approximately $7 \mu\text{m}$ in diameter is much larger than the sidewall and can, thus, generate carriers both in the QWR and in the QWs around it. Figures 4(b) and 4(c) compare PLE spectra by detecting the emission of the QW_{HH} (detection energy 1.546 eV) and of the QWR_{HH} (1.521 eV) resonances, respectively. In the former case, the two peaks in the emission intensity are attributed to the electron-heavy-hole (QW_{HH}) and electron-light-hole (QW_{LH}) transitions of the QW at 1.548 and 1.558 eV, respectively. This assignment is consistent with calculations of the energy levels for a 10-nm-thick QW with $\text{Al}_{0.15}\text{Ga}_{0.85}\text{As}$ barriers.

The QWR_{HH} PLE spectrum in Fig. 4(c) also shows an onset at the QWR_{HH} transition as well as two excitation maxima blue shifted by 4 and 5 meV with respect to the QW_{HH} and QW_{LH} transitions, respectively. These blue-shifted lines are assigned to the electron-heavy-hole and electron-light-hole transitions in the barrier QW. Carriers excited in the barrier QW can then diffuse to the QWR and recombine in the QWR. The absence of a peak in the PLE spectrum of Fig. 4(c) corresponding to the QW_{HH} transition as observed in Fig. 4(b) implies that for excitation energies above approximately 1.542 eV, the detected QWR PL arises from the recombination of electron-hole pairs photoexcited in the barrier-QW region, which diffuse into the QWR. Carriers generated in the QW, in contrast, cannot reach the QWR due to the energy barrier imposed by the barrier QW. For excitation energies below 1.542 eV we expect that the QWR PL results from a combination of direct excitation of QWR states as well as of the low-energy flank of the barrier QW.

We analyze the carrier dynamics by performing time-resolved PL measurements using a streak camera while exciting the sample using 1.5-ps pulses from a Ti:sapphire laser emitting at a wavelength of 790 nm. Figure 5 shows the PL intensity as a function of energy (horizontal axis) and time (vertical axis) recorded by focusing a $3\text{-}\mu\text{W}$ laser beam onto a $7\text{-}\mu\text{m}$ -wide laser spot on a sidewall under an angle of 45° . We observe emission from the sidewall QWR (1.520 eV), QW (1.546 eV), as well as from the GaAs substrate (1.514 eV). The right panel shows temporal traces extracted from the image for the QW resonance (blue, thin line) and QWR (red, thick line) by spectral integration of the PL over the linewidth of the corresponding resonances.

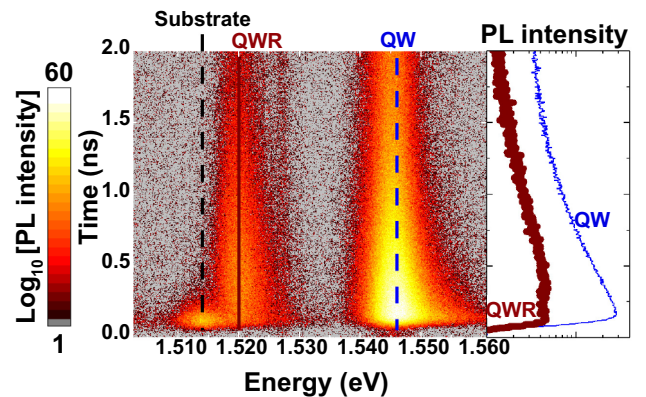


FIG. 5. Time-resolved PL traces recorded on a ridge sidewall as a function of emission energy (horizontal axis) and time (vertical axis). The three observed resonances are (from the low energy to the high energies) the electron-heavy-hole transitions in the GaAs substrate (1.514 eV, dashed black line), sidewall QWR (1.520 eV, solid red line), and QW (1.546 eV, dashed blue line). The right panel shows the temporal trace of the QW (blue, thin) and QWR (red, thick). Both traces represent spectral integrations over the linewidth of the respective emission lines.

In contrast to the substrate signal, which exponentially decays with a time constant of only 70 ps, the PL from the QW and QWR persists for times exceeding 1 ns. In both cases, the formation of large- k_{\parallel} excitons from excited electron-hole pairs leads to the initial fast rise of the PL intensity and blue shift of the emission line. These excitons then relax into a state with $k_{\parallel} = 0$ and subsequently recombine with the emission of a photon [27]. From a single-exponential fit we extract a QW carrier lifetime of approximately 500 ps.

The temporal emission trace of the QWR shows an initial fast increase followed by a plateau (or even a small increase) in the emission up to approximately 400 ps. The signal then decreases exponentially with a time-decay constant of approximately 870 ps. The larger recombination lifetime of the QWR states with respect to the QW is attributed to the larger thickness of the QWR [28]. We attribute the plateau to the transfer of carriers from the surrounding barrier QW into the QWR. The initial rise time can be explained by the fast carrier transfer from the barrier QW as well as by direct excitation of carriers in the QWR, while the plateau can be explained by the diffusion and relaxation of barrier-QW carriers into the QWR states. A similar process is reported for carrier transfer in the nanosecond timescale between QWs and sidewall QWRs on GaAs(113)A substrates [29]. Note that although the bulk emission is spectrally closely located to the QWR, its fast decay implies only a minor contribution to the PL signal.

E. Acoustic transport

We provide in this section experimental evidence for acoustic charge transport along the sidewall QWRs, obtained by spatially resolved PL spectroscopy. The experiments are carried out using the configuration sketched in the right panels of Fig. 6. The carriers are photoexcited by a pulsed diode laser (635 nm, power 2 μ W) focused onto a spot with a diameter of 6 μ m at the reference position $y = 0$ μ m. A metal stripe is deposited at the end of the QWR (at $y = 90$ μ m) to block the acoustic transport. Since the depth of the QWR (below a 200-nm Al_{0.15}Ga_{0.85}As barrier) is much smaller than the SAW wavelength ($\lambda_{\text{SAW}} = 5.6$ μ m), the metal efficiently screens the SAW piezoelectric potential at the depth of the QWR and induces the recombination of the carriers transported by the SAW field [20]. In the ideal case, one thus expects to observe PL at two positions along the SAW path: (i) at the excitation location, where nontransported carriers recombine and (ii) at the metal-stripe position due to recombination of transported carriers. Furthermore, in the present case, the metal stripe consists of a stack of 10-nm titanium, 30-nm aluminium, and 10-nm titanium layers. Using the optical transmission data taken from Ref. [30], we calculate an optical transmittance of only 0.8% at the QWR emission ($\lambda = 815.8$ nm).

We expect, therefore, to collect only the PL emitted by carriers recombining along the transport path and at the edges of the metal stripe. The small optical transmittance of the metal stripe should suppress PL from directly below the metal stripe. Despite that, we show that we can still detect PL at the borders of the opaque metal stripes. In future investigations, semitransparent stripes will be used to increase the PL collection efficiency.

In the absence of SAW excitation, PL is only observed around the excitation spot [Fig. 6(a)]. The application of a weak SAW (−7 dBm) induces electron-hole transport along both the QW and the QWR, as illustrated in Fig. 6(b). This image shows that the PL intensity at the excitation location reduces under a SAW. This is attributed to the storage of the carriers by the moving SAW piezoelectric potential, which transports them away from the excitation location. Additionally, the image shows a strong remote PL emission at approximately 30 μ m before the metal stripe, which we attribute to carrier trapping and recombination by a trapping center within the transport channel. The trap captures carriers of one polarity, which then recombine upon the arrival of carriers of opposite polarity in the subsequent SAW half cycle.

Interestingly, remote PL is observed at the same y coordinate for both the QWR and the QW resonances. We remind ourselves that carrier transfer between the QW and the QWR is hindered by the barrier QW inbetween them. In addition, we show in Sec. III B that only carriers generated in the barrier QW can diffuse to the QWR, and that this process takes place within a nanosecond. Considering the acoustic transport velocity of 2.9 μ m ns^{−1}, this transfer between the barrier QW and the QWR can only take place during the first couple of micrometers of the transport path. The simultaneous remote emission from the QW and QWR could be due to an extended defect blocking carrier transport along both the QW and QWR. Alternatively, if the acoustic transport in the QWR is blocked by a defect center, carriers can accumulate close to the defect and eventually leak to the QW.

The transport becomes more efficient at larger acoustic intensities, as shown by Figs. 6(b)–6(d). Here, a further increase of the acoustic intensity reduces the PL at the excitation location, because the increased SAW potential stores and transports electrons and holes more efficiently. A further interesting aspect is that remote trapping and recombination along the transport channel can be controlled by the acoustic intensity. The images in Figs. 6(b) and 6(c) show that an increase of the acoustic power to −2 dBm leads initially to an enhancement of the trap emission. After a certain power level, however, the emission from the trap becomes completely suppressed [Fig. 6(d)]. The SAW piezoelectric field becomes, in this case, sufficiently strong to overcome the trapping potential and transport the carriers all the way to the edge of the metal stripe 90- μ m away from the excitation spot. Note that the SAW power

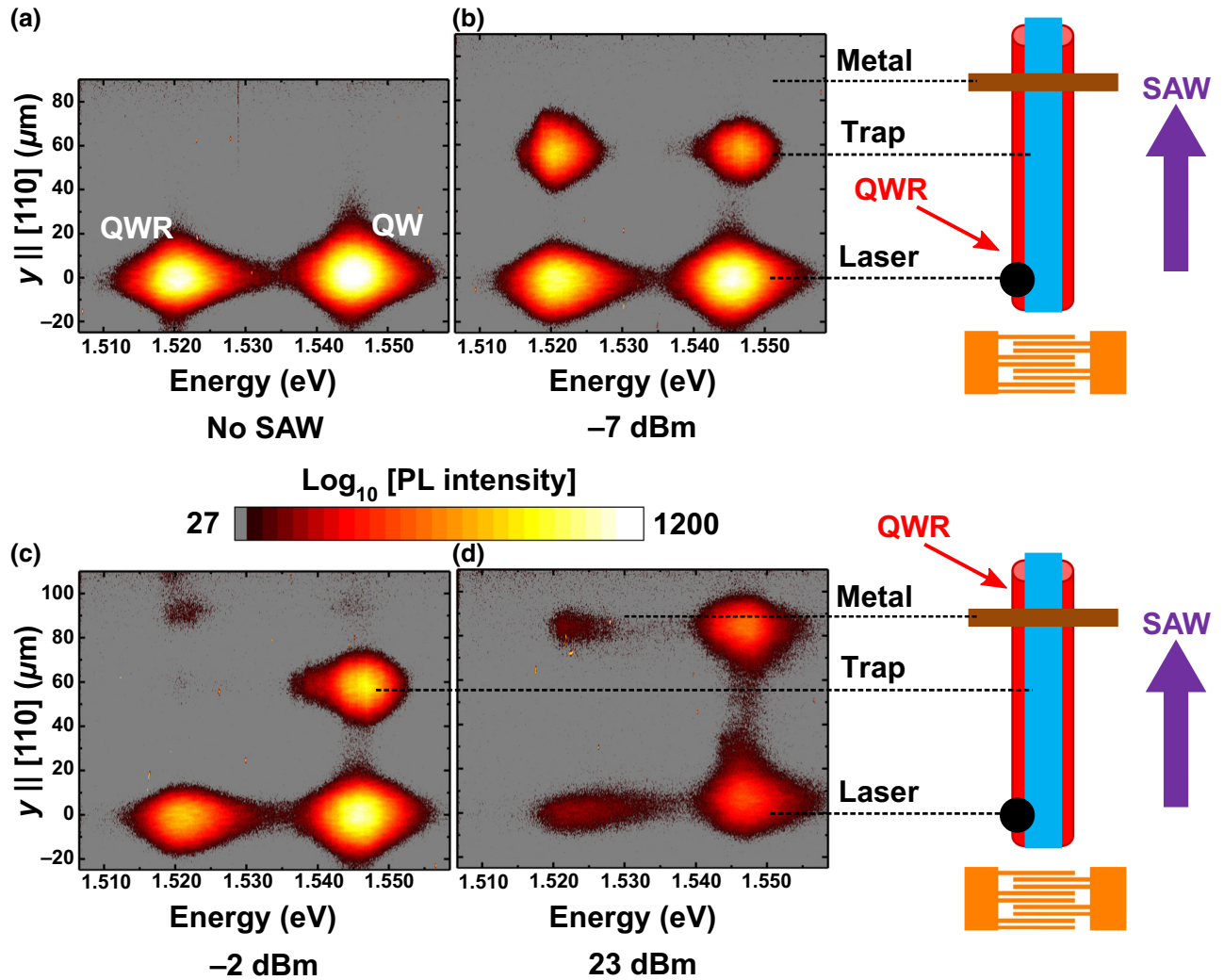


FIG. 6. Acoustic transport of photoexcited charge carriers in sidewall QWRs and surrounding QW. The figures show PL maps recorded using the configuration in the right panels without SAW (a) and with SAWs with nominal powers of (b) -7 , (c) -2 , and (d) 23 dBm. The carriers are excited with a 635 -nm laser focused to a spot of approximately $6 \mu\text{m}$ diameter on a ridge sidewall. The carriers are transported by the SAW field to a trapping center or, for high acoustic powers, up to a metal stripe, which induces recombination by quenching the SAW piezoelectric field.

threshold for overcoming the trap potential is different for transport along the QWR and QW. At the metal-stripe position, the piezoelectric field is screened, leading to the recombination of transported carriers. However, as mentioned before, due to the small optical transmission of 0.8% of the metal stripe, we expect to only observe a small fraction of the PL at this position. Additionally, for very high SAW powers the piezoelectric field is only partially screened and therefore the carriers are potentially transported further along the SAW path (out of the measurement area).

Figure 7 displays PL maps recorded by selectively exciting carriers in the QWR using an excitation energy (1.537 eV) below the QW resonance. In this case, the acoustic transport takes place only along the QWR. In the absence

of a SAW [Fig. 7(a)] PL from the QWR is only observed at the excitation spot near a weak emission line from the GaAs substrate. When a SAW is applied [$\lambda_{\text{SAW}} = 4 \mu\text{m}$, $f_{\text{SAW}} = 726$ MHz, cf. Fig. 7(b)], one detects PL at two trapping sites on the QWR, thus evidencing acoustic transport. The upper panel displays PL spectra of the two trapping sites. The spectrum from trap A (red) resembles the QWR emission at the excitation spot (1.521 eV). A similar spectral behavior is found for most of the trapping centers – a model of this type of trap centers is presented below. In contrast, the trapping center at site B shows a narrower emission line (linewidth of 2 meV in comparison with 7 meV for trap A), which is blue shifted by 4 meV with respect to the PL at the excitation location.

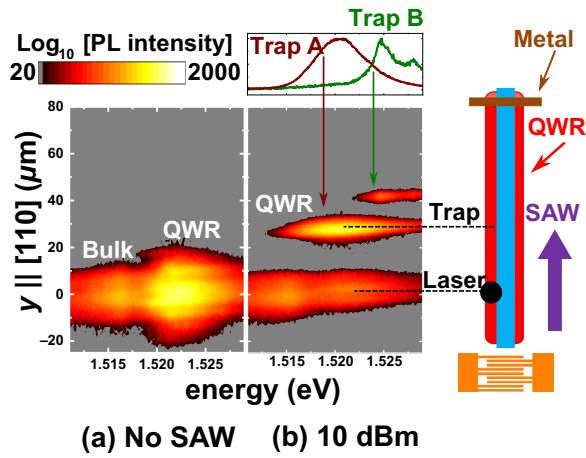


FIG. 7. Spatially resolved PL maps recorded (a) in the absence of a SAW and (b) under a SAW with a frequency of 726 MHz and nominal rf excitation power of 10 dBm. The carriers are selectively excited in the QWR at $y = 0$ (cf. right panel) using a laser beam tuned to an energy ($E_{\text{laser}} = 1.537$ eV) below the band gap of the surrounding QW. Under acoustic excitation, the carriers are transported along the wire and recombine in two trapping centers (A and B) with spectral emissions displayed in the upper panel.

As mentioned in Sec. III B, a 31-meV potential barrier protects the QWR carriers from escaping into the surrounding QW. In the following, we show that the SAW piezoelectric field can extract carriers from the QWR into the surrounding QW. This behavior is observed close to trapping centers, as illustrated in Figs. 8(a)–8(f). Figure 8(a) shows for reference the PL spectrum extracted from Fig. 6(a), which is obtained by exciting the ridge sidewall at an energy above the QW resonance. Figures (b) and (c) display PL maps of three QWRs recorded by selectively exciting the center QWR. The excitation energy is red shifted with respect to the QW resonance and the PL, spectrally integrated over the QWR resonance, is collected in the absence and presence of a SAW, respectively. The excitation energy as well as the collected PL energy range are indicated in Fig. 8(a). In the absence of a SAW [cf. Fig. 8(b)], QWR PL is only observed close to the excitation location $y = 0$ μm with a diffusion tail along the QWR. Under a SAW [Fig. 8(c)], one observes remote PL in the excited QWR at recombination centers at $y = 10$ and $y = 28$ μm , which are labeled as trap 1 and trap 2 in the schematic diagram in Fig. 8(d). In addition, remote PL is also observed in a neighboring QWR at $y = 19$ μm (trap 3), thus indicating that carriers excited in a QWR can be extracted to the QW and diffuse towards a neighboring QWR.

Further evidence for the extraction process is provided by PL maps recorded by collecting the QW emission, as displayed in Figs. 8(e) and 8(f). The weak PL observed close to the excitation spot in the absence of a SAW [Fig.

8(e)] is possibly related to an anti-Stokes PL excitation process [31]. The QW emission increases significantly under a SAW, as is shown in Fig. 8(f): this emission concentrates around the trapping centers with enhanced remote QWR PL, thereby confirming the SAW-induced extraction of carriers from the QWR to the QW. Although further studies will be needed to elucidate the extraction process, we note that the energy to overcome the potential barrier between the QWR and the QW can be provided by the SAW piezoelectric potential, which can reach hundreds of mV.

F. Time-resolved acoustic transport

The dynamics of the acoustic transport is studied by time-resolved PL. The carriers are optically excited using a small spot (diameter of approximately 3 μm) and a cw Ti:sapphire laser (wavelength of 780 nm and power of 200 μW). The remote PL induced by the acoustic transport of carriers to a trap within the QWR is collected and detected using a Si avalanche detector (temporal resolution of 340 ps) synchronized with the SAW phase. Figure 9 shows the PL time dependence recorded on a trap located approximately 30 μm away from the excitation spot. The cw PL spectrum of the trap (inset) reveals that it is similar to trap A in Fig. 7(b) emitting at the same energy as the QWR. The PL intensity oscillates at the SAW frequency of 726 MHz. For comparison, the blue curve displays the vanishing PL intensity collected in the absence of SAW, which proves that the trap is only populated by acoustically transported carriers.

The strong oscillations in the time-resolved trace of Fig. 9 proves that the carriers remain confined within the SAW potential during acoustic transport (note that the amplitude of the oscillations in Fig. 9 is only marginally affected by the time resolution of the avalanche detector, since the QWR carrier lifetime is approximately three times larger than the time resolution). In addition, the frequency of the oscillations yields information about the carrier trapping and recombination process. In fact, one expects PL oscillations at the SAW frequency only if the trapping center captures carriers of only one polarity during one half of the SAW cycle, followed by recombination upon arrival of carriers with the opposite polarity in the subsequent half of the SAW cycle. The capture (and subsequent recombination) of carriers of both polarities results, in contrast, in PL oscillations at twice the SAW frequency. In the present experiments, we cannot discriminate which carriers (electrons or holes) are preferentially trapped.

Our experimental data supports the model for carrier trapping and recombination during ambipolar transport proposed in Ref. [32]. In this model, carriers of one polarity are trapped due to injection into states at the GaAs/Al_{0.15}Ga_{0.85}As interface by the vertical component E_z of the SAW piezoelectric field. The field-induced injection probability is high since, for a Rayleigh SAW,

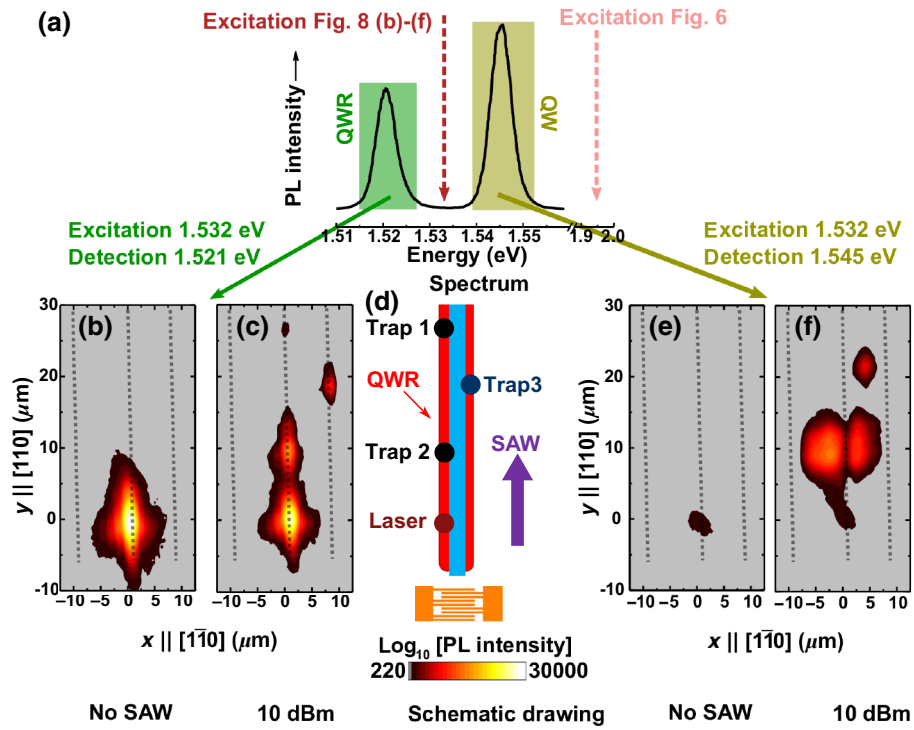


FIG. 8. SAW-mediated extraction of carriers from the QWR into the surrounding QW. (a) PL spectrum of the ridge sidewall displaying the emission lines from the QWR and QW [cf. Fig. 6(a)]. (b),(c) PL maps obtained by collecting the QWR emission induced by an excitation energy of 1.532 eV (excitation power of $100 \mu\text{W}$), without SAW (b) and with a SAW of 10 dBm (c). The collected PL range as well as the excitation energy are indicated in (a). The dashed lines schematically depict the positions of the QWRs in the figure. Figure (c) shows emission from a remote recombination center in the excited QWR (trap 1) as well as from a remote recombination center in a neighboring QWR (trap 3), as indicated in the schematic diagram in (d). (e),(f) Corresponding PL maps recorded by collecting the QW emission [cf. Fig. (a)], which is blue shifted with respect to the excitation energy. The strong QW PL under acoustic excitation proves that the SAW can extract carriers from the QWR into the surrounding QW.

E_z is in phase with the piezoelectric potential and, therefore, with the maximum in the carrier density. E_z reverses its sign half a SAW cycle later, thus releasing the trapped

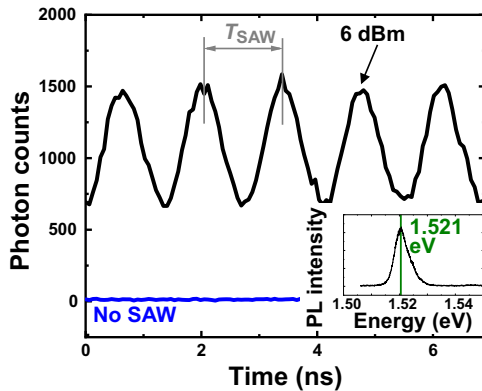


FIG. 9. Time-resolved remote PL measured on a trap with the spectral emission displayed in the inset. The trap is populated by carriers transported by a SAW with a wavelength of $4 \mu\text{m}$, frequency 726 MHz, and nominal rf excitation power of 6 dBm. The blue curve shows, for comparison, the PL trace in the absence of a SAW.

carriers into a pool of carriers of the opposite polarity, where it has a high recombination probability. This mechanism thus leads to efficient recombination during acoustic transport with emission energy equal to the QWR. This model can account for the emission behavior of most of the trapping sites detected along the acoustic transport path (i.e., of type A, cf. Fig. 7). In previous acoustic transport studies in sidewall QWRs on GaAs(113)A, the experimental conditions (in particular, the acoustic power) could be adjusted to control carrier trapping and induce the appearance of narrow spectral lines along the QWR axis [19,32,33]. A similar experimental situation could not be reproduced in the GaAs(001) QWRs studied here, where the observed recombination centers are separated by several μm . While further studies are required to elucidate the different behaviors, we speculate that they may arise from the different QWR dimensions and nature of the interfaces for the two crystallographic directions.

IV. CONCLUSIONS

We study structural, optical, and transport properties of sidewall QWRs fabricated on patterned GaAs(001)

substrates. QWRs formed by overgrowth of a 10-nm-wide QW on prepatterned ridges have thickness and width of approximately 25 and 200 nm. The sidewall QWRs form on both sides of the ridges aligned along the [110] crystal direction and exhibit similar emission properties at both sides of the ridges. Their emission is spectrally red shifted by 27 meV with respect to the fundamental transition of the QW. The linewidth of the QWR emission lines of 10.5 meV is slightly increased with respect to the QW. One source of potential fluctuations contributing to the QWR linewidth are fluctuations in the lateral dimensions of the QWRs, as is implied by the increased linewidth of the QWR with respect to the QW. By combining S(T)EM and AFM measurements, we estimate that the amplitude of line-edge-roughness is small as compared to the QWR lateral width. LER is therefore expected to play only a minor role in the acoustic transport of carriers. Furthermore, LER is mainly caused by the photolithography process.

We further demonstrate that photoexcited electrons and holes can be acoustically transported along the QWR over distances of at least 90 μm . By selectively exciting carriers using a laser energy below the band gap of the surrounding QW, we prove that the majority of the QWR carriers is transported along the QWR and not via the surrounding QW. The transport distances are in many cases limited by the presence of trapping centers along the transport channel, which block the transport and induce recombination of the carriers. These traps have been observed both in the QW and the sidewall QWR. The majority of the traps in the QWR exhibits emission energies and linewidths comparable to the ones expected for the QWR. Some of the traps can, however, exhibit much narrower linewidth (down to approximately 2 meV) and a slightly different emission energy. The submicrometer widths, the efficient lateral confinement and acoustic transport properties of the sidewall QWRs on GaAs(001) substrates make them a promising candidate for interconnections of charge and spin carriers in semiconductor structures.

ACKNOWLEDGMENTS

We thank Jens Herfort for a critical reading of the manuscript, as well as W. Anders, A. Tahraoui, and S. Rauwerdink for help in the fabrication of the samples. This project has received funding from the European Union's Horizon 2020 research and innovation program under Grant Agreement No. 642688.

-
- [1] G. Fasol and H. Sakaki, Electron-Electron Scattering in Quantum Wires and its Possible Suppression due to Spin Effects, *Phys. Rev. Lett.* **70**, 3643 (1993).
 [2] A. A. Kiselev and K. W. Kim, Progressive suppression of spin relaxation in two-dimensional channels of finite width, *Phys. Rev. B* **61**, 13115 (2000).

- [3] A. W. Holleitner, V. Sih, R. C. Myers, A. C. Gossard, and D. D. Awschalom, Suppression of Spin Relaxation in Submicron InGaAs Wires, *Phys. Rev. Lett.* **97**, 036805 (2006).
 [4] A. Hernández-Mínguez, K. Biermann, R. Hey, and P. V. Santos, Electric control of spin transport in GaAs (111) quantum wells, *Phys. Rev. B* **94**, 125311 (2016).
 [5] Loren Pfeiffer, H. L. Störmer, K. W. Baldwin, K. W. West, A. R. Goñi, A. Pinczuk, R. C. Ashoori, M. M. Dignam, and W. Wegscheider, Cleaved edge overgrowth for quantum wire fabrication, *J. Cryst. Growth* **127**, 849 (1993).
 [6] R. Bhat, E. Kapon, D. M. Hwang, M. A. Koza, and C. P. Yun, Patterned quantum well heterostructures grown by OMCVD on non-planar substrates: Applications to extremely narrow SQW lasers, *J. Cryst. Growth Special Issue J. Crystals Growth* **93**, 850 (1988).
 [7] E. Kapon, D. M. Hwang, and R. Bhat, Stimulated Emission in Semiconductor Quantum Wire Heterostructures, *Phys. Rev. Lett.* **63**, 430 (1989).
 [8] S. Koshiba, H. Noge, H. Akiyama, T. Inoshita, Y. Nakamura, A. Shimizu, Y. Nagamune, M. Tsuchiya, H. Kano, and H. Sakaki, *et al.*, Formation of GaAs ridge quantum wire structures by molecular beam epitaxy on patterned substrates, *Appl. Phys. Lett.* **64**, 363 (1994).
 [9] Y. Horikoshi, T. Uehara, T. Iwai, and I. Yoshida, Area selective growth of GaAs by migration-enhanced epitaxy, *Phys. Status Solidi (b)* **244**, 2697 (2007).
 [10] J. Lee, Z. Wang, B. Liang, W. Black, V. P. Kunets, Y. Mazur, and G. J. Salamo, Formation of self-assembled sidewall nanowires on shallow patterned GaAs (100), *IEEE Trans. Nanotechnol.* **6**, 70 (2007).
 [11] R. Nötzel, J. Menniger, M. Ramsteiner, A. Ruiz, H-P. Schönherr, and K. H. Ploog, Selectivity of growth on patterned GaAs (3 1 1)A substrates, *Appl. Phys. Lett.* **68**, 1132 (1996).
 [12] R. Nötzel, M. Ramsteiner, J. Menniger, A. Trampert, H-P. Schönherr, L. Däweritz, and K. H. Ploog, Patterned growth on high-index GaAs (n11) substrates: Application to sidewall quantum wires, *J. Appl. Phys.* **80**, 4108 (1996).
 [13] R. Nötzel, Z. C. Niu, M. Ramsteiner, H-P. Schönherr, A. Trampert, L. Däweritz, and K. H. Ploog, Uniform quantum-dot arrays formed by natural self-faceting on patterned substrates, *Nature (London)* **392**, 56 (1998).
 [14] C. Rocke, S. Zimmermann, A. Wixforth, J. P. Kotthaus, G. Böhm, and G. Weimann, Acoustically Driven Storage of Light in a Quantum Well, *Phys. Rev. Lett.* **78**, 4099 (1997).
 [15] P. V. Santos, M. Ramsteiner, and F. Jungnickel, Spatially-resolved photoluminescence in GaAs surface acoustic wave structures, *Appl. Phys. Lett.* **72**, 2099 (1998).
 [16] K. Biermann, O. D. D. Couto, Jr., W. Seidel, R. Hey, and P. V. Santos, Electronic channels for acoustic transport in semiconductor heterostructures, *Appl. Phys. Lett.* **96**, 162106 (2010).
 [17] F. Alsina, P. V. Santos, H-P. Schönherr, W. Seidel, R. Nötzel, and K. H. Ploog, Surface-acoustic-wave-induced carrier transport in quantum wires, *Phys. Rev. B* **66**, 165330 (2002).
 [18] F. Alsina, P. V. Santos, H. P. Schönherr, R. Nötzel, and K. H. Ploog, Real-time dynamics of the acoustically-induced carrier transport in GaAs quantum wires, *Phys. Rev. B* **67**, 161305(R) (2003).

- [19] F. Alsina, J. A. H. Stotz, R. Hey, U. Jahn, and P. V. Santos, Acoustic charge and spin transport in GaAs quantum wires, *Phys. Status Solidi C* **9**, 2907 (2008).
- [20] F. Alsina, P. V. Santos, H.-P. Schönherr, R. Nötzel, and K. H. Ploog, Real-time dynamics of the acoustically driven electron-hole transport in GaAs quantum wires, *Phys. E* **21**, 430 (2004).
- [21] H. Sanada, Y. Kunihashi, H. Gotoh, K. Onomitsu, M. Kohda, J. Nitta, P. V. Santos, and T. Sogawa, Manipulation of mobile spin coherence using magnetic-field-free electron spin resonance, *Nat. Phys.* **9**, 280 (2013).
- [22] R. P. Mirin, I-H. Tan, H. Weman, M. Leonard, T. Yasuda, J. E. Bowers, and E. L. Hu, InGaAs quantum well wires grown on patterned GaAs substrates, *J. Vac. Sci. Technol. A: Vacuum, Surfaces, Films* **10**, 697 (1992).
- [23] Y. Horikoshi, M. Kawashima, H. Yamaguchi, and M. Sato, in *Semiconductor Interfaces at the Sub-Nanometer Scale* (Springer Netherlands, 1992) p. 1.
- [24] V. P. LaBella, D. W. Bullock, Z. Ding, C. Emery, W. G. Harter, and P. M. Thibado, Monte Carlo derived diffusion parameters for Ga on the GaAs(001)-(2 × 4) surface: A molecular beam epitaxy scanning tunneling microscopy study, *J. Vac. Sci. Technol., A* **18**, 1526 (2000).
- [25] R. M. White and F. W. Vollmer, Direct piezoelectric coupling to surface elastic waves, *Appl. Phys. Lett.* **7**, 314 (1965).
- [26] Chris A. Mack, in *Proc. SPIE 7639, Advances in Resist Materials and Processing Technology XXVII*, 763931 (2010).
- [27] T. C. Damen, Jagdeep Shah, D. Y. Oberli, D. S. Chemla, J. E. Cunningham, and J. M. Kuo, Dynamics of exciton formation and relaxation in GaAs quantum wells, *Phys. Rev. B* **42**, 7434 (1990).
- [28] E. O. Göbel, H. Jung, J. Kuhl, and K. Ploog, Recombination Enhancement due to Carrier Localization in Quantum Well Structures, *Phys. Rev. Lett.* **51**, 1588 (1983).
- [29] Ch. Lienau, A. Richter, G. Behme, M. Süptitz, D. Heinrich, T. Elsaesser, M. Ramsteiner, R. Nötzel, and K. H. Ploog, Nanoscale mapping of confinement potentials in single semiconductor quantum wires by near-field optical spectroscopy, *Phys. Rev. B* **58**, 2045 (1998).
- [30] Mikhail N. Polyanskiy, Refractive index database, <https://refractiveindex.info> (2018).
- [31] Roberto Cingolani and Klaus Ploog, Frequency and density dependent radiative recombination processes in III–V semiconductor quantum wells and superlattices, *Adv. Phys.* **40**, 535 (1991).
- [32] S. Lazić, R. Hey, and P. V. Santos, Mechanisms for non-classical light emission from acoustically populated (3 1 1)A GaAs quantum wires, *New J. Phys.* **14**, 013005 (2012).
- [33] O. D. D. Couto, Jr., S. Lazić, F. Iikawa, J. Stotz, R. Hey, and P. V. Santos, Photon anti-bunching in acoustically pumped quantum dots, *Nat. Phot.* **3**, 645 (2009).